Anharmonic motion of a trapped ion under the influence of different drives in an ion-nanomechanical hybrid system

Adrien Poindron and Stefan Willitsch*

Department of Chemistry, University of Basel, Klingelbergstrasse 80, 4056 Basel, Switzerland

(Received 4 February 2026; accepted 12 June 2026; published 7 July 2026)

Ions in traps hybridized with nanomechanical oscillators represent promising platforms for studying interactions between microscopic and macroscopic systems and for manipulating the classical and quantum motion of trapped particles. In a previous report [Weegen *et al.*, Phys. Rev. Lett. **133**, 223201 (2024)], we presented a hybrid system combining laser-cooled trapped ions with an oscillating and electrically charged nanowire driving the ion motion. Here, we focus on the ramifications of trap-potential anharmonicites introduced by the nanooscillator and show that the driven classical motion of the ions in this hybrid system obeys Duffing-type dynamics. We combine electrical and mechanical drives to explore the details of the anharmonic ion motion and demonstrate how anharmonicity and damping parameters can be determined from analyzing the steady-state amplitude and phase of the motion under these conditions. The present results provide new insights into the dynamical properties of ion-nanomechanical hybrid systems and the anharmonic motion of trapped particles under the influence of different types of drives.

DOI: 10.1103/mw5k-p3gg

I. INTRODUCTION

Cold trapped ions [1] are among the most precisely controlled quantum systems available today with applications ranging from frequency metrology and clocks [2–4], over force sensing [5,6], quantum information [7,8], to collision studies and chemistry [9,10]. Their high degree of controllability makes them ideal candidates for their combination with other physical systems, e.g., neutral atoms or other types of ions, where they can serve as interaction partners or as sensitive probes for their counterparts [10–13]. Simultaneously, nano- and micromechanical oscillators have emerged as a versatile platform for a range of applications [14–16]. Available as clamped [17–19], levitated [20–23], or membrane-type devices [24–26], they are candidates for hybridization with other systems in order to realize a crossover between the microscopic and the macroscopic realms. Thus, nanomechanical hybrid systems constitute new platforms for the exploration of interactions with atoms and molecules [14,23,27–29], for new approaches to quantum-state engineering [30,31], and for the realization of accurate measurements of weak interactions [32].

We have recently presented a hybrid experiment in which single trapped ions are electrostatically coupled to an oscillating clamped nanowire [19,33]. In this previous work, we explored the resonant driving of the ion motion by the mechanical action of the nanowire. We also discussed how the presence of the nanowire introduces anharmonicities into the trapping potential of the ion. Trap anharmonicities, regardless of whether they originate from the trap design [6,34,35], are introduced by the environment [19,36,37], or are generated from the trapped charges themselves [38,39], play a crucial role in the classical [36,40] and quantum [30,41–43] dynamics of the confined ions.

In our ion-nano-oscillator hybrid system, anharmonicities in the trapping potential invariably arise by the introduction of the nanowire into the trap [33]. While these trap anharmonicities did not manifest themselves in our previously reported experiments [19], we show here that they represent an important feature of the present hybrid system and that the classical ion motion in our experiment can be described as a driven anharmonic oscillator obeying a Duffing-type equation [36,44]. We explore the anharmonic motion of the ion under the action of both an electrical and the mechanical drive and demonstrate how anharmonicity and damping parameters for the hybrid system can be determined by mutually canceling both drives. The results obtained with this new method to determine Duffing parameters are in excellent agreement with those obtained from both conventional approaches and numerical simulations of the trap potential.

II. THEORY

A. Periodic drives

In the present experiments, the trapped-ion oscillator was driven by two types of forces originating either from an oscillating electric field applied to a nearby trap electrode (dubbed "tickle") [45] or from the charged nanowire oscillator that was itself mechanically driven by a piezoelectric actuator [19,33]. The forces exerted by the tickle (F_{tkl}) and the

*Contact author: stefan.willitsch@unibas.ch

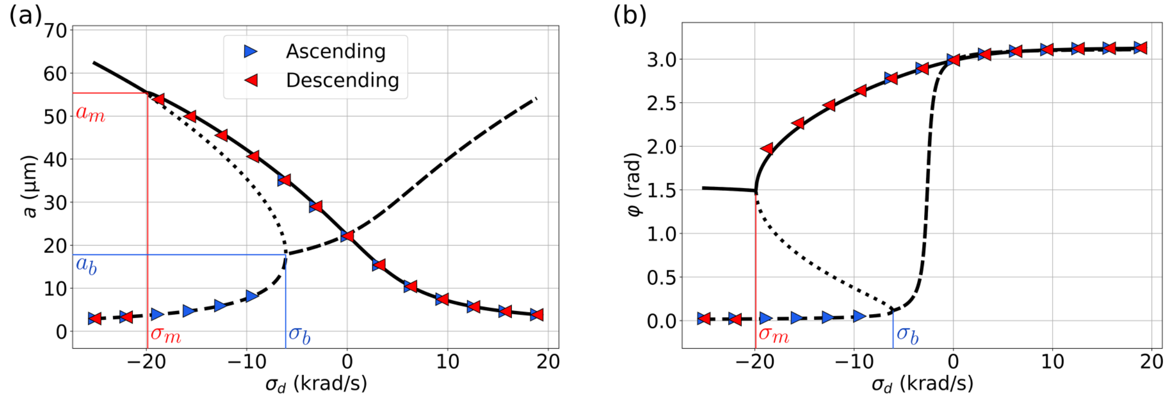

FIG. 1. Dynamics of the Duffing oscillator. Steady-state (a) amplitude a and (b) phase φ of the oscillator as a function of the angular-frequency detuning σ_d of the drive. The solid and dashed lines represent stable analytical solutions of Eq. (3), and the dotted line represents the unstable solution. The colored triangles represent numerical solutions of Eq. (3). Parameters used: $k_d = 9.67 \times 10^4\ \mathrm{rad^2\ m\,s^{-2}}$, $\omega_0 = 2\pi \times 4.225 \times 10^5\ \mathrm{rad\ s^{-1}}$, $\alpha = -4.720 \times 10^{19}\ \mathrm{rad^2\ m^{-2}\,s^{-2}}$, $2\mu = 7.01 \times 10^2\ \mathrm{rad\ s^{-1}}$, $\gamma = 1.18 \times 10^{-1}\ \mathrm{rad\ m^{-2}\ s}$, $\delta = -12.44\Gamma$, $\varphi_d = 0$. See text and Appendices D and E for details.

nanowire (F_{nw}) can be written as $F_{\mathrm{tkl}} = A_{\mathrm{tkl}} \cos(\omega_{\mathrm{tkl}} t + \varphi_{\mathrm{tkl}})$ and $F_{\mathrm{nw}} = A_{\mathrm{nw}} \cos(\omega_{\mathrm{nw}} t + \varphi_{\mathrm{nw}})$, respectively. Here, A_i denotes the amplitude, ω_i the angular frequency, and φ_i the phase of the drive $i \in \{\mathrm{tkl}, \mathrm{nw}\}$.

When both forces are applied together, each with the same amplitude $A_{\mathrm{nw}} = A_{\mathrm{tkl}} = A_d$ and frequency $\omega_{\mathrm{nw}} = \omega_{\mathrm{tkl}} = \omega_d$, an analytical model for the combined drive can be derived in the steady-state regime (see Appendix A) such that the resulting driving force $F_d = F_{\mathrm{tkl}} + F_{\mathrm{nw}}$ can be written as

$$F_d = A_d \sqrt{2(1 + \cos \Delta\varphi_d)}\ \cos\left(\omega_d t + \frac{\Delta\varphi_d}{2}\right), \quad (1)$$

where $\Delta\varphi_d$ is the relative phase between the two drives. For $\Delta\varphi_d = 0$, F_d scales as $2A_d$. When $\Delta\varphi_d$ increases up to π, F_d decreases until it reaches 0 when the driving forces are applied in opposition, effectively canceling each other.

B. Anharmonic ion motion in the trap

We now consider the one-dimensional dynamics of a laser-cooled ion in a linear radiofrequency (rf) ion trap [46] with an anharmonic effective trap potential along the longitudinal (x) trap axis. Expanding the trap potential in a Taylor series up to fourth order and taking into account only even terms in the series expansion on grounds of symmetry (see Appendix B), modeling laser cooling as a friction force (see Appendix C) and including a periodic driving force as described in the previous section results in a Duffing-type equation [44] for the classical motion of the ion in the trap,

$$\ddot{x} + 2\mu\dot{x} + \gamma\dot{x}^3 + \omega_0^2 x + \alpha x^3 = k_d \cos(\omega_d t + \varphi_d). \quad (2)$$

Here, μ and γ are the linear and cubic damping coefficients, respectively, associated with the laser-cooling force [47], $k_d = A_d/m$, where m is the mass of the ion, ω_0 is the harmonic angular oscillation frequency of the ion in the trap, and α is the coefficient associated with the leading, quartic anharmonicity term of the potential (see Appendix B). The higher-order terms in both the potential and the friction force in Eq. (2) have an increasing effect as the amplitude of the oscillator increases. They are often neglected in a first-order treatment [46], but will be of importance in the present study. The even terms in the velocity have not been included because they can be accounted for with rescaled odd terms [48–50].

The different parameters occurring in Eq. (2) can, in principle, be determined theoretically through numerical simulations of the trapping and interaction potentials, as well as assuming an analytical model for the laser cooling. Alternatively, they can also be determined experimentally by the following procedure.

Defining the frequency detuning of the drive from the resonance frequency ω_0 as $\sigma_d = \omega_d - \omega_0$, the steady-state amplitude a of the ion oscillator can be obtained from the solution of Eq. (2) as [36,44]

$$\frac{k_d^2}{4\omega_0^2} = \left[\left(\sigma_d - \frac{3\alpha}{8\omega_0}a^2\right)^2 + \left(\mu + \frac{3}{8}\gamma\omega_0^2 a^2\right)^2\right]a^2. \quad (3)$$

As a sixth-order polynomial with only even powers of a, Eq. (3) has three distinct solutions, among which one is unstable under small perturbations [44]. These solutions are plotted as a function of the drive detuning σ_d in Fig. 1(a) as lines, while triangles represent numerical results obtained from molecular-dynamics simulations (see Appendix D). The solid and dashed lines represent the two stable solutions, while the dotted line is the unstable solution. The unstable solution superimposes with one of the stable solutions when the detuning satisfies either $\sigma_d \leqslant \sigma_m$ or $\sigma_d \geqslant \sigma_b$, where $\sigma_m = 3\alpha a_m^2/(8\omega_0)$ and $\sigma_b = 9\alpha a_b^2/(8\omega_0)$, rendering that solution locally unstable and leaving only the other stable dynamics for the oscillator. σ_m and σ_b thus denote boundaries for the detuning in between which there are two valid stable solutions with different amplitudes. Here, a_m and a_b denote the maximum oscillation amplitudes before the relevant transition points (see Fig. 1).

The coexistence of these two solutions gives rise to a hysteresis behavior as evidenced in Fig. 1. When varying the detuning, the oscillator always evolves according to a stable solution of Eq. (3) in a continuous manner until the dynamics coincides with the unstable solution. At this point, the oscillator transitions to the other stable solution at either σ_m or σ_b depending on whether the drive frequency is continuously decreased or increased during the experiment (red and blue triangles, respectively, in Fig. 1).

$\sigma_{m,b}$ and $a_{m,b}$ can thus be determined experimentally from a measurement of the steady-state oscillator amplitude a as a function of the detuning σ_d according to Fig. 1(a). The potential parameters ω_0 and α can be expressed as a function of these measurable parameters as

$$\omega_0 = \frac{a_m^2\omega_b - 3a_b^2\omega_m}{a_m^2 - 3a_b^2}, \tag{4}$$

$$\alpha = \frac{8\omega_0(\sigma_m - \sigma_b)}{3(a_m^2 - 3a_b^2)}. \tag{5}$$

Once ω_0 and α are determined, Eq. (3) has three remaining unknowns μ, γ, and k_d. As all parameters associated with the damping terms in Eq. (2) are grouped together in the second term on the right-hand side of Eq. (3), the following change of variable can be carried out to effectively reduce the number of unknown parameters:

$$\mu' = \mu + \tfrac{3}{8}\gamma\omega_0^2 a^2. \tag{6}$$

The measured values for (a_m, σ_m) and (a_b, σ_b) can then individually be applied to Eq. (3), yielding a system of two equations that can be solved for the two unknowns μ' and k_d. Finally, by making a hypothesis on either μ or γ using, respectively, Eq. (C4) or (C5) of Appendix C, the remaining unknown variable can be determined from Eq. (6). Note that making a hypothesis on μ will provide more reliable results as this parameter is disconnected from the amplitude in Eq. (6).

The steady-state phase of the ion oscillator relative to the phase of the drive is given by [44]

$$\tan\varphi = \frac{(\mu + 3\gamma\omega_0^2 a^2/8)8\omega_0}{3\alpha a^2 - 8\omega_0\sigma_d}. \tag{7}$$

Note that this phase explicitly depends on the amplitude of the motion a. Figure 1(b) shows the solution of Eq. (7) for each solution of Eq. (3) as a function of the drive detuning σ_d. This figure shows again the characteristic hysteresis behavior induced by the coexistence of two stable solutions within a limited range of driving frequencies bounded by σ_m and σ_b.

III. EXPERIMENTAL METHODS

The details of the experiment have been described previously [19,33]. Briefly, single $^{40}Ca^+$ ions were trapped in a segmented linear rf ion trap with an electrode-to-electrode distance of 400 μm and an rf of 21.629 MHz applied to two diagonally opposed electrodes. The trap was interfaced with an AgGa nanowire of length ≈16 μm and diameter ≈150 nm mounted on a tungsten tip. The nanooscillator was held at a variable electrical potential V_{nw} and positioned at a distance of ≈230 μm from the ion using nanopositioners. Its vibration was resonantly driven by a piezoelectric actuator to which an oscillating voltage of amplitude V_{piezo} was applied. The strength of the mechanical drive on the ion was adjusted by varying either V_{nw} or V_{piezo} [19].

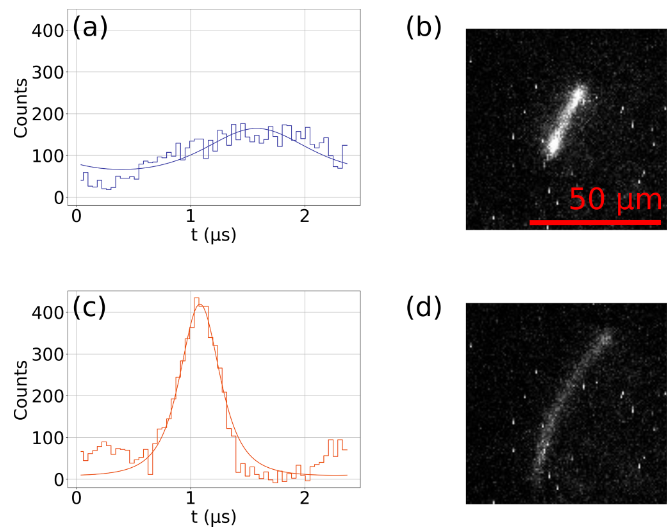

FIG. 2. Histograms of the time-resolved laser-cooling fluorescence of a single Ca^+ ion in the trap under the action of (a) a weak and (c) a strong drive for one period of oscillation and the corresponding camera images [panels (b) and (d)]. Histograms correspond to 20 000 photon counts collected in 250 bins. Background photon counts collected during an experiment were subtracted. Solid lines represent fits of the histograms to Eq. (C1). Camera images show the ion fluorescence integrated over 0.5 s, illustrating the steady-state amplitude a of the ion motion in both experiments.

Static potentials were applied to the trap endcaps to confine the ion along the longitudinal trap axis. The potentials were chosen such that an angular resonance frequency around $\omega_0 = 2\pi \times 422$ krad/s was obtained for the ion oscillation along the trap axis coinciding with an eigenfrequency of the nanowire. The ion was Doppler laser cooled using a 397 nm laser beam to drive the cooling transition $(4s)^2S_{1/2} \rightarrow (4p)^2P_{1/2}$ and a 866 nm laser beam to repump population on the transition $(3d)^2D_{3/2} \rightarrow (4p)^2P_{1/2}$. The laser-cooling fluorescence of the ion at 397 nm was collected through a microscope objective and divided with a 50:50 beam splitter to be directed to both a photomultiplier tube (PMT) and a camera. Driven motion of the ion was characterized using the photon-correlation technique [19,33,51]. Under the action of a drive, the ion velocities oscillate. The ion therefore experiences oscillating Doppler shifts and, consequently, scattering rates. From measurements of the time-resolved fluorescence of the ion [Figs. 2(a) and 2(c)], its maximum velocity during the oscillation was retrieved [33]. Generally, the amplitude of the oscillations in the time-resolved fluorescence traces increases with the amplitude of the ion motion due to the concomitant increase of the maximum Doppler shift. This is illustrated in Figs. 2(a)–2(d) that show time-resolved photon counts and camera images of an ion under weak and strong drives, respectively. The position of the maximum of the histogram is related to the phase of the oscillator, which, in turn, is correlated with the amplitude of oscillation in accordance with Eq. (7). Precise, effective detunings δ_0 of the 397 nm cooling laser were also determined using the photon-correlation method as discussed in Ref. [52].

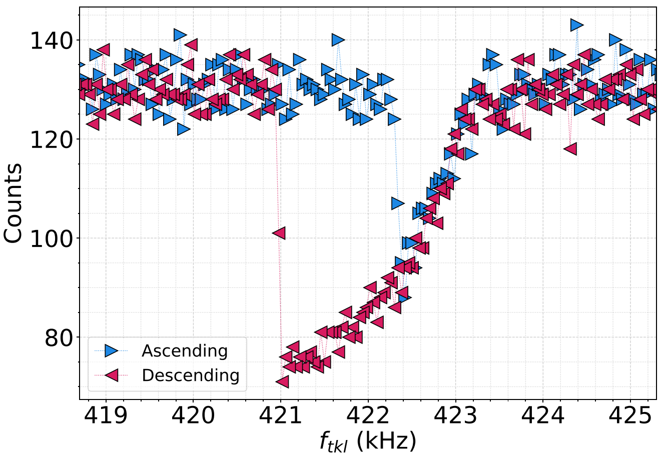

FIG. 3. Laser-cooling fluorescence as a function of the frequency $f_{\rm tkl}$ of an applied electrical drive. Each triangle represents an average of ten fluorescence measurements collected over 0.1 s each. The blue (red) triangles represent ascending (descending) frequency sweep directions. The hysteresis is visible in the frequency interval between 421.0 and 422.30 kHz. See text for details.

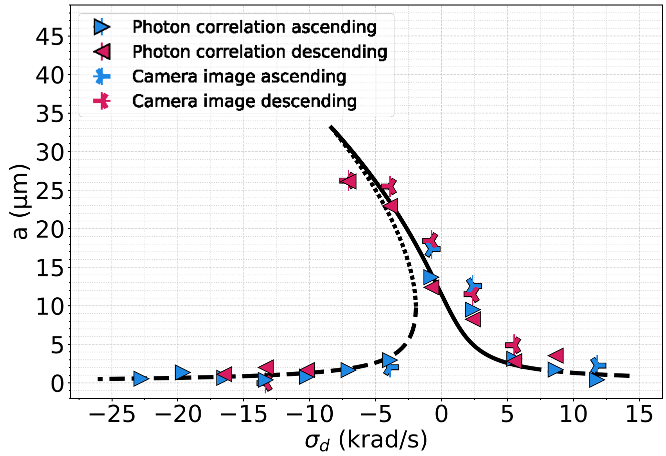

FIG. 4. Steady-state amplitude a of the ion oscillator as a function of the detuning σ_d. Triangles and three-armed crosses represent amplitudes derived from the photon-correlation measurements and camera images, respectively. Lines indicate analytical amplitudes computed using the experimentally determined Duffing parameters.

IV. RESULTS

A. Characterizing the Duffing oscillator using an electrical drive on the ion

Figure 3 shows the intensity of the time-averaged laser-cooling fluorescence collected by the PMT as a function of the frequency $f_{\rm tkl} = \omega_{\rm tkl}/(2\pi)$ of an applied electrical drive. The ion was driven with an oscillating electric field applied to a compensation electrode located above the trap. A marked decrease in the fluorescence could be observed in the region of resonance between 421 and 423 kHz. This decrease indicates a resonant excitation of the axial motion of the ion by the drive, resulting in a reduced scattering rate because of the increased average speed, and hence oscillation amplitude, of the ion. The fluorescence counts were measured as a function of the drive frequency swept in both ascending and descending directions. The fluorescence profiles clearly show the hysteresis behavior discussed in Sec. II B with two distinct discontinuities in the fluorescence yield at 421.0 ± 0.023 kHz and 422.3 ± 0.023 kHz depending on the sweep direction corresponding to $\sigma_m/(2\pi)$ and $\sigma_b/(2\pi)$, respectively.

The corresponding oscillation amplitudes of the ion, $a_m = (36.4 \pm 1.16)$ µm and $a_b = (9.40 \pm 1.16)$ µm, were retrieved from camera images such as the ones shown in Figs. 2 (b) and 2(d). Using Eqs. (4) and (5), these measurements allowed to determine the potential parameters $\omega_0 = 2\pi \times (422.62 \pm 0.17)$ krad s^{-2} and $\alpha = (-5.39 \pm 0.91) \times 10^{19}$ krad^2 m^{-2} s^{-2}.

Inserting both (σ_m, a_m) and (σ_b, a_b) into Eq. (3), the system of equations was solved for μ' and k_d, yielding $\mu' = 359.12$ rad s^{-1} and $k_d = (69\,429 \pm 12\,643)$ rad^2 m s^{-2}. Equation (C4) was then used to estimate the linear damping parameter μ. In these experiments, the detuning was set to $\delta_0 = -8.36\Gamma$ and the saturation parameter of the cooling laser derived from its intensity was $s_0 = 7.02$. The linear damping parameter was thus obtained as $\mu = (566 \pm 62)$ rad s^{-1}, which finally gives $\gamma = (-5.92 \pm 1.78) \times 10^{-2}$ m^{-2} rad s.

We can now compare the steady-state amplitude a of the ion as a function of σ_d obtained from the solutions of Eq. (3) and the parameters just determined to the experimental ion oscillation amplitudes measured under these conditions. Figure 4 shows the amplitude computed from Eq. (3) as black lines. The data points represent experimental amplitudes extracted either from camera images (three-armed crosses) or using the photon-correlation method (triangles). For the latter approach, the maximum velocities have been determined from the photon-count histograms from which steady-state oscillation amplitudes were then retrieved using Eq. (B4). It can be seen from Fig. 4 that the agreement between the theoretical prediction and the experiment is generally good. The discrepancy between the experimental data and the theory at the highest amplitudes is likely caused by the influence of additional anharmonicites in the potential, which are not incorporated in the potential model of Eq. (2). These also manifest themselves in a bending of the trajectory of the ion at very high amplitudes, as can be seen in Fig. 2(d). In addition, an onset of saturation of the signal in the photon-correlation measurements was observed under these conditions as the amplitude of the oscillation of the ion started to exceed the width of the cooling laser beam.

As can be seen in Fig. 4, the current theoretical treatment is accurate up to ion oscillation amplitudes of about 20 µm above which deviations of the theory from experiment become noticeable. To account for these deviations at large amplitudes, the theory can be improved systematically by including higher-order terms in the series expansion of both the potential and the damping force in Eq. (2), however, at the expense of increasing the numbers of free parameters.

B. Conditions for canceling combined electrical and mechanical drives

We now explore specific experimental conditions for balancing both drives, i.e., $F_d = F_{\rm nw} - F_{\rm tkl} = 0$ as discussed in Sec. II A. During this experiment, the voltage $V_{\rm piezo}$ of the

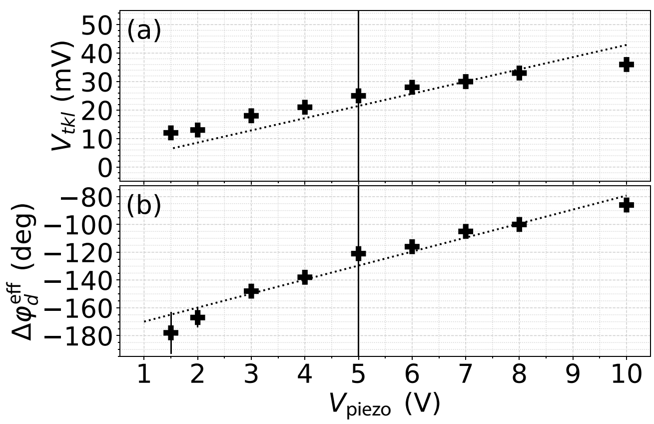

FIG. 5. Conditions for balancing the electrical and mechanical drives. (a) Tickle voltage V_{tkl} as a function of the nanowire piezo-drive voltage V_{piezo} required to balance the drives. (b) Effective relative phase $\Delta\varphi_d^{\mathrm{eff}}$ between the individual drives needed to balance the combined drives as a function of the piezo voltage of the nanowire. The dashed lines are linear fits. The vertical black line through both panels indicates the drive amplitude used for subsequent experiments to determine the Duffing parameters. See text for details.

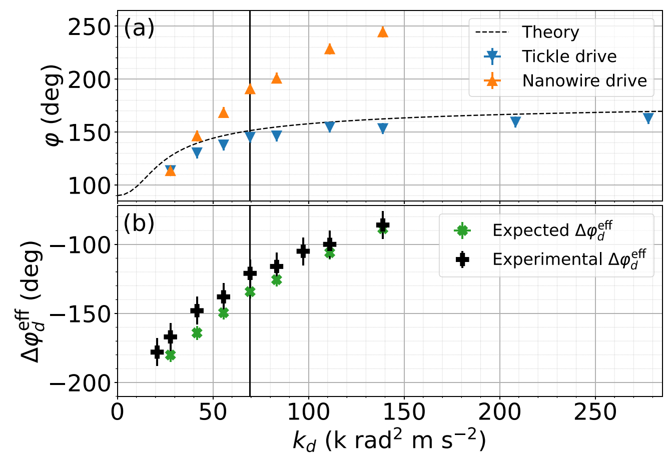

FIG. 6. (a) Steady-state phase φ of the motion of the trapped ion determined from photon-correlation measurements as a function of the amplitude k_d of the electric tickle (blue triangles) and nanowire (orange triangles) drives. The dashed line indicates the theoretical phase computed from Eq. (7) corrected for instrument-related phase shifts. (b) Differences $\Delta\varphi_d^{\mathrm{eff}}$ between the phases of the ion oscillator induced by the two drives as a function of the drive amplitude k_d (green crosses) and experimentally determined relative phase needed to cancel the drives [black crosses corresponding to the data displayed in Fig. 5(b)]. The vertical black line in both panels indicates the drive amplitude used in subsequent experiments to determine the Duffing parameters; see text for details. Error bars represent the standard deviation of five measurements, except for the black data points, where they represent the empirical uncertainty with which the optimal phase can be determined from the analysis of the camera images.

piezo actuating the nanowire was increased from 0 to 10 V, while the tickle voltage V_{tkl} and the relative phase between the drives were adjusted in order to minimize the amplitude of oscillation of the ion. Figures 5(a) and 5(b) illustrate the corresponding combinations ensuring a minimization of the oscillation amplitude of the ion on the camera images. $\Delta\varphi_d^{\mathrm{eff}}$ is the relative phase between the two drives required in the experiment in order to effectively satisfy the theoretical cancelation condition $\Delta\varphi_d = 180^\circ$ discussed in Sec. II A. Note that the effective relative phase required to cancel the drives increases with the drive amplitude [Fig. 5(b)]. While at small drive amplitudes, a value $\Delta\varphi_d^{\mathrm{eff}} \approx 180^\circ$ was found, for $V_{\mathrm{piezo}} = 5$ V a phase difference $\Delta\varphi_d^{\mathrm{eff}} \approx -135^\circ$ was required for cancelation. The dependency of the effective cancelation phase $\Delta\varphi_d^{\mathrm{eff}}$ on the drive amplitude k_d is attributed to Eq. (7) that states that the steady-state phase of the driven ion motion φ depends on its amplitude a and, therefore, on the drive amplitude k_d. Interestingly, the results shown in Fig. 5 imply that this dependency is different for both drives, otherwise $\Delta\varphi_d^{\mathrm{eff}}$ would be constant over a change in V_{piezo}. For different drive amplitudes, different values for $\Delta\varphi_d^{\mathrm{eff}}$ have to be chosen to achieve cancelation as shown in Fig. 5(b).

To explore this point further, the phase of the ion as a function of the drive amplitude k_d was measured for each drive individually using the photon-correlation method. As the photon-correlation histograms are only sensitive to the ion velocity, 90° were subtracted from the measured values to account for the phase offset between velocity and position. As can be seen in Fig. 6(a), the phase of the ion under the tickle drive is closely following the theoretical phase (dashed curve) obtained from Eq. (7) with the present experimental parameters and correcting for phase shifts generated by the electronics of the experiment. In contrast, the phase of the ion under the action of the nanowire drive exhibits a different dependency on the drive amplitude. Thus, in order to cancel the drives, different effective relative phases $\Delta\varphi_d^{\mathrm{eff}}$ between them have to be chosen depending on the amplitude to achieve the nominal condition $\Delta\varphi_d = 180^\circ$ in Eq. (1). Figure 6(b) shows the effective relative drive phases $\Delta\varphi_d^{\mathrm{eff}}$ needed to cancel the drives as a function of the amplitude k_d. The black crosses represent the experimentally determined relative phases needed to minimize the ion motional amplitude corresponding to the data displayed in Fig. 5(b). These coincide with the green crosses that represent the differences of the phases of the individual drives displayed in Fig. 6(a) (blue and orange triangles). These results reinforce the conclusion that the phase of the ion seems to have a different response to the nanooscillator compared to the tickle drive.

C. Duffing dynamics under combined electrical and mechanical drives

We now demonstrate an alternative approach to experimentally determine the salient dynamical parameters of the Duffing oscillator, which is based on the conditions to balance the combined electrical and mechanical drives. With both drives set to equivalent amplitudes, the relative phase $\Delta\varphi_d$ between them was varied by changing the relative phase of the nanowire drive with respect to the tickle from -45° to 60° in steps of 15°. In this experiment, the tickle-drive amplitude was set to $V_{\mathrm{tkl}} = 25$ mV, which is equivalent to a value of $k_d = A_d/m = 69\,429$ rad^2 m s^{-2} (determined according to the procedure described in Sec. IV A). The voltage applied

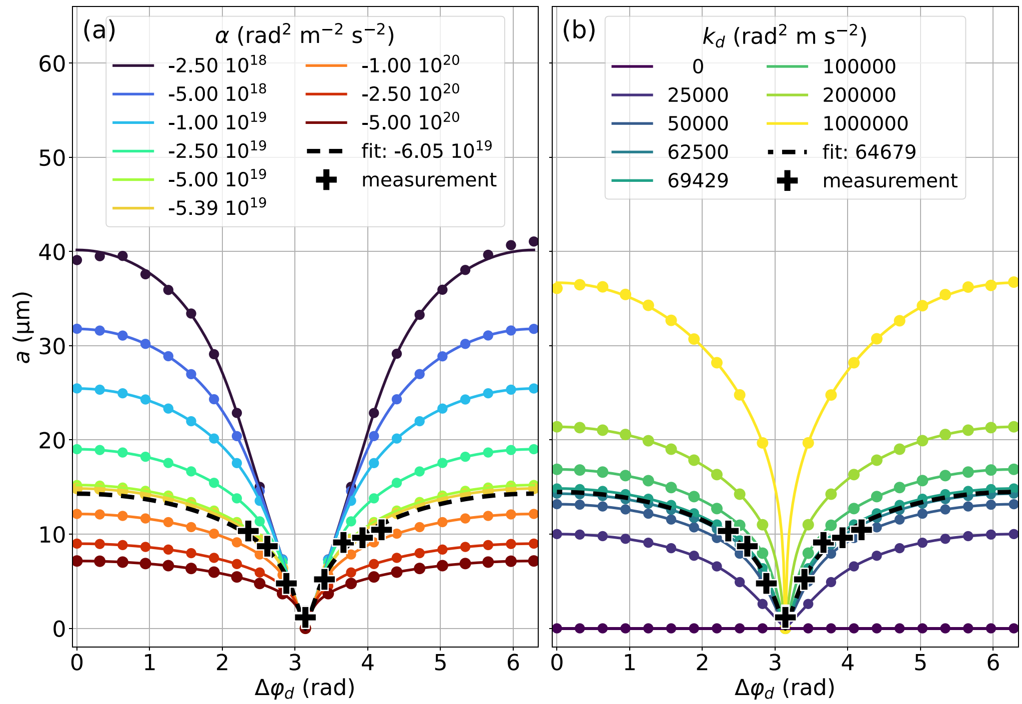

FIG. 7. Duffing-oscillator dynamics as a function of the phase difference between the two drives. Steady-state amplitude a of the ion motion as a function of the relative phase $\Delta\varphi_d$ of the two drives plotted for (a) different anharmonicity parameters α and (b) different drive amplitudes k_d. The lines and points represent analytical and numerical solutions of the ion dynamics, respectively. The crosses represent measurements and the dashed line a fit to the experimental data. Data points correspond to the average of ten measurements; error bars are smaller than the symbols.

to the nanowire piezo required to balance this tickle drive was $V_{\text{piezo}} = 5$ V. Under these conditions [indicated by the solid vertical lines in Fig. 5(b)], an effective relative phase of $\Delta\varphi_d^{\text{eff}} = -135^\circ$ had to be applied between the drives to perfectly cancel them.

The relative phase $\Delta\varphi_d$ between the drives was now varied and at each step, photon-correlation traces of the ion were measured. The data were fitted to Eq. (C1) to retrieve the maximum velocity of the ion from which the steady-state amplitude a of its motion was computed using Eq. (B4). The data are presented in Fig. 7. Here, $\Delta\varphi_d$ was renormalized by adding -135° to ensure that cancelation of the drives occurs at the theoretical value $\Delta\varphi_d = 180^\circ$ according to Eq (1). The experimental results are compared to both numerical (colored dots) and analytical solutions (colored lines) of Eq. (2) for various values of the anharmonicity parameter α [Fig. 7(a)] and the drive amplitude k_d [Fig. 7(b)]. In both panels, the numerical amplitudes were determined from molecular dynamics simulations (Appendix D) while the theoretical amplitudes were computed by solving Eq. (3) with a drive amplitude of the form $k_d = A_d/m\sqrt{2(1+\cos\Delta\varphi_d)}$ according to Eq. (1). The numerical amplitudes were obtained from the envelope of the analytic signal of the position in the steady-state regime (see Appendix E). The black dashed lines in Fig. 7 represent fits of the experimental data to the analytical solution [Eq. (3)] with all other (nonfitted) Duffing parameters fixed to the values previously determined in Sec. IV A.

Treating α as fit parameter in Fig. 7(a), the fit yields $\alpha = (-6.05 \pm 0.68) \times 10^{19}$ rad^2 m^{-2} s^{-2} close to the value $(-5.39 \pm 0.91) \times 10^{19}$ determined using the tickle drive in combination with image analysis in Sec. IV A. Fitting the drive amplitude k_d in Fig. 7(b), a value $k_d = (6.47 \pm 0.38) \times 10^5$ rad^2 m s^{-2} is obtained, again close to the value $k_d = (6.94 \pm 1.26) \times 10^5$ rad^2 m s^{-2} determined in Sec. IV A.

V. DISCUSSION

The nonlinear terms αx^3 and $\gamma \dot{x}^3$ in the Duffing equation (2) have an increasing effect as the amplitude and velocity of the oscillator increase. In most trapped-ion experiments, these terms are neglected because the ions are located close to the minimum of the trap potential at low temperatures, which ensures low oscillation amplitudes and velocities. However, in situations in which the trapped ion is significantly displaced from the minimum of the potential, these terms may play a significant role. This displacement may be due to the presence of other charges in the vicinity of the ion or, as in the present case, the action of the nanowire. The nanowire introduces a significant degree of anharmonicity in the trap [33], which gives rise to the hysteresis in the frequency-response curve.

As the nanowire can only be driven at certain fixed frequencies defined by its motional modes [19,33], the observation of the hysteresis behavior of the ion dynamics as a hallmark of a Duffing oscillator required an external drive (here, the electric tickle drive), the frequency of which could be continuously varied. As evidenced in Fig. 4, the response of the present ion oscillator to the drive deviates from harmonic behavior already at amplitudes as small as 5 µm reached for drive detunings below 5 krad/s. Furthermore, the nonlinear damping term $\gamma\dot{x}^3$ in Eq. (2) significantly affects the ion oscillation amplitudes at large displacements. A positive sign of γ implies stronger cooling at large velocities, which reduces the steady-state amplitude, while, as in the present case, a negative nonlinear damping coefficient implies reduced cooling as the velocity increases, increasing the steady-state amplitude. We attribute the negative sign of the cubic damping coefficient in the present experiments to the to reduced photon scattering due to larger Doppler shifts at larger velocities, thus reducing the efficiency of cooling.

For the present balanced double-drive experiment, hysteresis behavior does not play a role when varying the relative phase between the drives and a symmetrical response of the oscillation amplitude on the phase difference is observed (Fig. 7). As shown here, the quartic potential anharmonicity parameter α (or the drive amplitude k_d) can easily be determined from such a balanced double-drive experiment, provided all other parameters of the Duffing equation are known. We note that hysteresis behavior is in principle also observable when sweeping the drive amplitude [44], which can be avoided thanks to a careful choice of drive detuning (as was done in the double-drive experiment presented in Sec. IV B).

With respect to the estimation of the parameters of Eq. (2), care should be taken that the motional amplitude of the ion remains small with respect to the size of the laser beam, the extent of the trapping region, and the ion-nanowire distance such that the approximation of Eq. (2) remains valid. Otherwise, even higher terms in the series expansion of the potential and the damping need to be included. Note also that while the variable change introduced in Eq. (6) is convenient, it is only valid for a given ion-oscillation amplitude and a given set of the parameters μ, γ. Any change in the experimental conditions, especially a change in the amplitude, requires a recomputation of μ'.

An intriguing result of the present work is the observation of a different phase response of the ion oscillator to the two drives, as shown in Figs. 5 and 6. While the phase shift of the ion across the range of electric-tickle-drive amplitudes studied is in line with Eq. 7, the physical reason for the larger phase shift induced by the nanowire drive evident from Fig. 6 is currently unclear and remains to be rationalized. The present theoretical treatment invariably assumes that the phase of the drive is known and well defined at every instance. Experimentally, this is readily achieved for the electric tickle drive, and consequently, the phase response of the ion when driven by the tickle follows the form expected from theory [compare the dashed line versus the blue triangles in Fig. 6(a)]. In contrast, we cannot control the phase of the nanowire drive directly, but only the phase of the voltage of the piezo oscillator that drives the nanooscillator. Thus, phase differences can occur between the piezo voltage and the piezo, between the piezo drive and the nanowire, and between the nanowire drive and the ion. The stronger-than-expected dependence of the phase response of the ion on the strength of the nanowire drive as controlled by the piezo voltage [orange triangles in Fig. 6(a)] suggests that additional nonlinearities not accounted for in the present theory must play a role, possibly in the drive of the nanowire by the piezo, as well as in the motion of the nanomechanical oscillator itself [53]. Additional possibilities are terms in the ion-nanowire interaction which are not accounted for in the present treatment. Moreover, as the tickle drive is also in resonance with the nanowire oscillation, a resonant back action of the tickle drive on the nanowire is also conceivable. The tickle could thus effectively act as a secondary drive not only on the ion, but also on the nano-oscillator itself [54]. The further characterization of such effects transcends the scope of the present work and will be the subject of further studies.

We wish to emphasize, however, that the lack of knowledge of the exact phase behavior of the nanowire does not affect the reliability of the present drive cancelation technique. As discussed, the phase of the nanowire drive is always empirically set such that the both drives cancel effectively, which can be readily ascertained in the experiment by minimizing the amplitude of the driven ion motion as a function of the piezo drive phase at a given drive amplitude. The reliability of this approach is evidenced by the fact that the values for the Duffing parameters α and k_d obtained using the drive cancelation technique agree within their uncertainties with those obtained by just using the tickle drive, see Sec. IV C above. We also note that both sets of results for α are in good agreement with the value $\alpha = -4.58 \times 10^{-19}\,\mathrm{rad}^2\,\mathrm{m}^{-2}\,\mathrm{s}^{-2}$ determined from the numerical potentials computed for the trap including the nanowire [33]. The consistency of all these results supports the validity of the current drive-cancelation technique.

VI. SUMMARY AND CONCLUSIONS

In the present study, we explored the anharmonic motion of a trapped ion induced by the presence of a nanowire in the trap in an ion-nanomechanical hybrid system. We showed that the ion dynamics exhibits the hallmark hysteresis behavior of Duffing oscillators, which was exploited to characterize the trapping potential, the laser cooling, and the driving force acting on the ion. A simultaneous electrical and mechanical drive was used to control the amplitude of oscillation of the trapped ion outside of the hysteresis regime. A model was derived for the case of two drives with equal amplitudes and frequencies, and then implemented in the experiments correspondingly. With this scheme, it was possible to precisely tune the driving force acting on the ion by varying the relative phase between the drives without changing other drive characteristics. Furthermore, the properties of the anharmonic ion oscillator were determined from these experiments.

The present results yielded new insights into the dynamical properties of ion-nanomechanical hybrid systems and the anharmonic motion of trapped particles under the influence of different types of drives. They pave the way for further lines of inquiry, such as the dependence of the phase of the ion motion on the nanomechanical drive, which still needs to be rationalized. The present results also form an important prerequisite for future developments of the hybrid experimental platform. An exciting prospect is the laser cooling of the ion into the quantum regime, which will open up possibilities to manipulate its motional quantum state using the nanomechanical oscillator. In this context, the characterization of trap-potential anharmonicities as undertaken here is crucial for the engineering of nonclassical motional states, as explored in more detail theoretically in Ref. [30].

ACKNOWLEDGMENTS

We acknowledge Dr. A. Johnson and G. Holderied for technical support. We thank Prof. M. Poggio and Prof. Philipp Treutlein (Basel) for helpful discussions. The present work was supported by the Swiss National Science Foundation (Grant No. 200021_204123), the Swiss Nanoscience Institute, and the University of Basel.

DATA AVAILABILITY

The data that support the findings of this article are available from the corresponding author upon reasonable request.

APPENDIX A: FORCE ON THE ION ORIGINATING FROM A COMBINED ELECTRICAL-MECHANICAL DRIVE

Assuming that both driving forces $F_{\rm tkl}$ and $F_{\rm nw}$ exhibit stationary amplitudes, frequencies, and phases, and provided that both drive frequencies are nearly degenerate ($\omega_{\rm tkl} \approx \omega_{\rm nw}$), the combined drive can be formulated as a single driving force of the form [44]

$$F_d = A_d(t)\cos(\omega_d t + \varphi_d(t)), \tag{A1}$$

with

$$A_d(t)^2 = A_{\rm tkl}^2 + A_{\rm nw}^2 + 2A_{\rm tkl}A_{\rm nw}\cos\theta, \tag{A2}$$

$$\varphi_d(t) = \varphi_{\rm tkl} + \arctan\frac{A_{\rm nw}\sin\theta}{A_{\rm tkl} + A_{\rm nw}\cos\theta}, \tag{A3}$$

$$\theta = (\omega_{\rm nw} - \omega_{\rm tkl})t + \varphi_{\rm nw} - \varphi_{\rm tkl}. \tag{A4}$$

Here, $\theta = \varphi_{\rm nw} - \varphi_{\rm tkl} \equiv \Delta\varphi_d$. For the case of strictly identical drive frequencies, both the phase $\varphi(t)$ and the amplitude $A(t)$ are time independent. Defining the tickle frequency as a reference with $\varphi_{\rm tkl} = 0$ and assuming both drives exhibit equal amplitudes, $A_{\rm tkl} = A_{\rm nw} = A_d$, Eq. (A1) becomes Eq. (1).

For the force on the ion originating from the oscillation of the nanowire $F_{\rm nw}$, the interaction model discussed in Refs. [19,30] yields the amplitude,

$$A_{\rm nw} = -\frac{\varepsilon}{d_{\rm nw}^2}\left(1 - 3\frac{x_{\rm nw}^2}{d_{\rm nw}^2}\right)cV_{\rm piezo}, \tag{A5}$$

with $d_{\rm nw}$ the distance between the tip of nanowire and the ion, $x_{\rm nw}$ their distance along the axis parallel to the drive direction, and $\varepsilon = q_{\rm ion}q_{\rm nw}/(4\pi\varepsilon_0)$, where $q_{\rm ion}$ and $q_{\rm nw}$ are the electrical charges of the ion and the nanowire, respectively. $V_{\rm piezo}$ is the voltage applied to the piezo drive used to actuate the nanowire. The proportionality constant $c = 184.42$ was determined from numerical simulations of the interaction potential [19]. $q_{\rm nw} = 1.84 \times 10^{-15} V_{\rm nw}$ is the charge of the nanowire as a function of its electrical potential $V_{\rm nw}$ as determined from the numerical model.

APPENDIX B: ANHARMONIC POTENTIAL

The anharmonic effective trap potential along the longitudinal trap axis is described as a fourth-order polynomial of the form $V = Cx^2 + Bx^3 + Ax^4$ [55–57]. In a conservative potential, the classical dynamics of an oscillator is fully described by the equation $\mathbf{F} = q\mathbf{E}$ such that $\ddot{x} + \omega_0^2 x + \beta x^2 + \alpha x^3 = 0$,

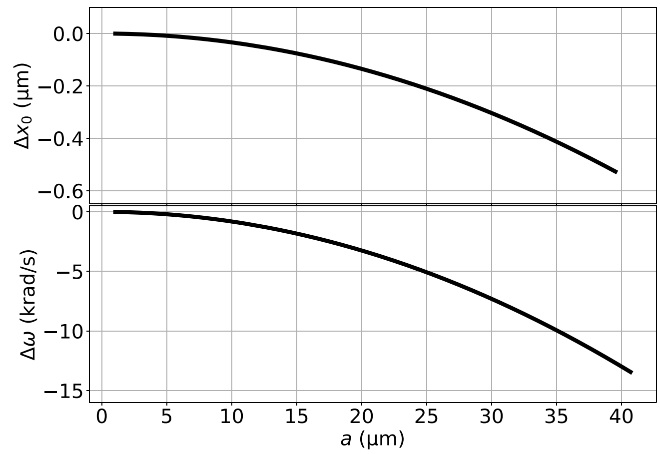

FIG. 8. Average displacement Δx_0 and frequency shift $\Delta\omega$ as a function of the amplitude a of an anharmonic oscillator. Parameters: $\omega_0 = 2\pi \times 42\,2500$ rad s^{-1}, $\alpha = -5.39 \times 10^{19}$ rad^2 m^{-2} s^{-2}, $\mu = 566$ rad s^{-1}, $\gamma = -5.92 \times 10^{-2}$ rad m^{-2} s. See text for details.

with ω_0 the harmonic angular frequency and β and α the coefficients associated with cubic and quartic potential anharmonicities, respectively [58].

The solution of this equation can be written as a sum of oscillating terms $x(t) = x^{(1)} + x^{(2)} + \cdots$ [59], such that

$$x^{(1)} = a\cos(\omega t + \varphi), \tag{B1}$$

$$x^{(2)} = \Delta x_0 - \frac{\Delta x_0}{3}\cos(2\omega t + \varphi). \tag{B2}$$

The average position of the oscillator is given by $\Delta x_0 = -\beta/(2\omega_0^2) \times a^2$. The angular frequency ω is obtained as

$$\omega = \omega_0 + \left(\frac{3\alpha}{8\omega_0} - \frac{5\beta^2}{12\omega_0^3}\right)a^2 = \omega_0 + \Delta\omega. \tag{B3}$$

The velocity of the ion $\dot{x} = \dot{x}^{(1)} + \dot{x}^{(2)} + \cdots$ is then calculated as

$$\dot{x}^{(1)} = -a\omega\sin(\omega t + \varphi), \tag{B4}$$

$$\dot{x}^{(2)} = -\frac{2\Delta x_0}{3}\omega\sin(\omega t + \varphi). \tag{B5}$$

The average position, the angular frequency, and the velocity all depend on the amplitude. The average displacement Δx_0 and the frequency shift $\Delta\omega = \omega - \omega_0$ are shown as a function of the amplitude in Fig. 8 for the experimental conditions relevant in this article.

For a typical asymmetry of $\beta = 3Bq/m = 4.75 \times 10^{15}$ rad^2 m^{-1} s^{-2} estimated using numerical simulations of the trap potential [33], and an amplitude of $a = 55$ µm, the displacement is $\Delta x_0 = -1.02$ µm, and the frequency shift is $\Delta\omega_0 = -21.6$ krad s^{-1} in accordance with the numerical values from Fig. 1. As the quartic potential term is responsible for >90% of the frequency shift, the cubic potential term is deemed negligible in the present experimental situation.

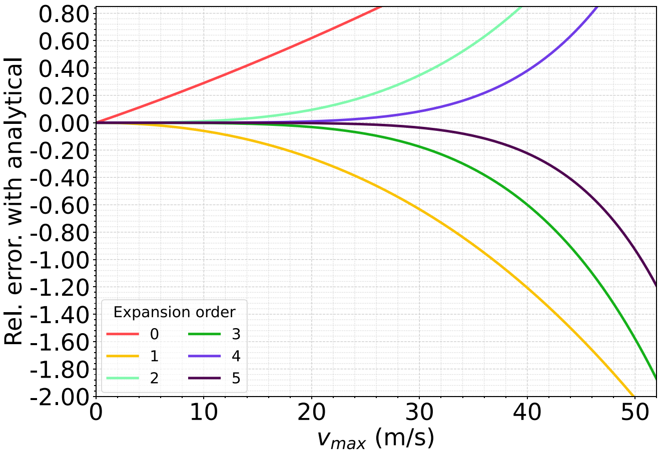

FIG. 9. Relative deviation of the scattering rate calculated with this series expansion in varying orders from the full analytical expression Eq. (C1). Parameters used: $\delta = -8.36\Gamma$, $s_0 = 7.02$.

APPENDIX C: SCATTERING RATE

The scattering rate of an ion under the action of laser cooling is given by [47,60]

$$R_s(\mathbf{v}) = \frac{\Gamma}{2} s_0 \frac{1}{1 + s_0 + 4\left(\frac{\delta(\mathbf{v})}{\Gamma}\right)^2} \tag{C1}$$

$$= \frac{\Gamma}{2} s_0 r_s(\mathbf{v}), \tag{C2}$$

with $\delta(\mathbf{v}) = \omega_l - \omega_0 - \mathbf{kv} = \delta_0 - \mathbf{kv}$ the laser detuning, $s_0 = I/I_{\text{sat}}$, $I_{\text{sat}} = \hbar\omega_0^3\Gamma/(12\pi c^2)$ the saturation parameter, and Γ the decay rate of the excited state. The scalar product $\mathbf{kv}$ can be expressed as a function of the maximum velocity $v_{\max}$ of the ion (its velocity amplitude), such that $\mathbf{kv} = 2\pi/\lambda \times v_{\max} \cos(\omega t + \varphi) \cos \widehat{\mathbf{kv}}$. In order to determine the friction parameters in Eq. (2), Eq. (C1) is expanded as a third-order Taylor expansion in $\mathbf{v}$ so that the coefficients in Eq. (2) can be identified,

$$\begin{aligned} R_s(\mathbf{v}) = s_0 \Bigg(& \frac{\Gamma}{2} r_s^0 \\ & + \frac{4\delta_0}{\Gamma} r_s^{0\,2} \mathbf{kv} \\ & - \frac{2}{\Gamma}\left(1 + s_0 - 12\left(\frac{\delta_0}{\Gamma}\right)^2\right) r_s^{0\,3} \mathbf{k}^2\mathbf{v}^2 \\ & - \frac{32\delta_0}{\Gamma^3}\left(1 + s_0 - 4\left(\frac{\delta_0}{\Gamma}\right)^2\right) r_s^{0\,4} \mathbf{k}^3\mathbf{v}^3 \\ & + \mathcal{O}(\mathbf{v}^4)\Bigg) \end{aligned} \tag{C3}$$

with $r_s^0 = r_s(\mathbf{v} = \mathbf{0})$. Figure 9 shows the relative deviation of the scattering rate calculated with this series expansion in varying orders from the full analytical expression Eq. (C1). Only considering the Taylor expansion up to first order (which is usually the standard treatment [46,47,60]), the deviation from the exact rate under the present conditions is already 20% at a velocity of 18 m/s.

As the force exerted by the laser on the ion is $F_s(\mathbf{v}) = \hbar k_l R_s(\mathbf{v})$, the coefficients of Eq. (2) can be identified with those of Eq. (C3). This yields

$$2\mu = -\frac{\hbar k_l^2}{m} s_0 \frac{4\delta_0}{\Gamma} r_s^{0\,2}, \tag{C4}$$

$$\gamma = \frac{\hbar k_l^4}{m} s_0 \frac{32\delta_0}{\Gamma^3}\left(1 + s_0 - 4\left(\frac{\delta_0}{\Gamma}\right)^2\right) r_s^{0\,4}. \tag{C5}$$

APPENDIX D: NUMERICAL METHODS

The Duffing equation (2) was solved numerically as the set of first-order differential equations,

$$\begin{aligned} \dot{x} &= v, \\ \dot{v} &= -\omega_0^2 x - \alpha x^3 - 2\mu v - \gamma v^3 + k_d \cos \omega_d t, \end{aligned} \tag{D1}$$

using a fifth-order Runge-Kutta algorithm [61,62] with a variable time step ensuring a tolerance of 10^{-6}. The simulations were split into three phases. First, the simulation was initialized for the given set of experimental parameters at a drive frequency outside the hysteresis region. Then, steady-state simulations were alternated with simulations in which a given parameter was smoothly varied. The numerical solutions were interpolated to 1000 data points for each period of the secular motion. The duration of the steady-state and smooth-sweep phases was chosen in order to avoid transitioning from the basin of attraction of one solution of Eq. (3) to another prematurely. The smooth sweeps used a hyperbolic tangent function [63] to transition between the two steady-state solutions.

APPENDIX E: ANALYTIC REPRESENTATION

A real-valued signal $s(t)$ is converted into its analytic representation $s_a(t)$ through the Hilbert transform H [64] such that

$$s_a(t) = s(t) + iH(s)(t). \tag{E1}$$

The amplitude of the real-valued signal is the envelope of the analytic signal and its phase φ is the argument of the analytic signal, such that

$$a = |s_a(t)|, \tag{E2}$$

$$\varphi = \arg s_a(t). \tag{E3}$$

This method was applied in the present study for the analysis of both the positions and the velocities obtained from the numerical simulations.

[1] In *Proceedings of the International School of Physics "Enrico Fermi"*, edited by M. Knoop, I. Marzoli, and G. Morigi (IOS Press, Amsterdam-Washington DC, 2015), Vol. 189.

[2] E. Peik, Optical atomic clocks, in *Photonic Quantum Technologies*, edited by M. Benyoucef (John Wiley & Sons, Ltd., Weinheim, Germany, 2023), Chap. 14, pp. 333–348.

[3] M. C. Marshall, Daniel A. Rodriguez Castillo, W. J. Arthur-Dworschack, A. Aeppli, K. Kim, D. Lee, W. Warfield, J. Hinrichs, N. V. Nardelli, T. M. Fortier, J. Ye, D. R. Leibrandt, and D. B. Hume, High-stability single-ion clock with 5.5×10^{-19} systematic uncertainty, Phys. Rev. Lett. **135**, 033201 (2025).
[4] H. N. Hausser, J. Keller, T. Nordmann, N. M. Bhatt, J. Kiethe, H. Liu, I. M. Richter, M. von Boehn, J. Rahm, S. Weyers, E. Benkler, B. Lipphardt, S. Dörscher, K. Stahl, J. Klose, C. Lisdat, M. Filzinger, N. Huntemann, E. Peik, and T. E. Mehlstäubler, $^{115}In^+ - ^{172}Yb^+$ Coulomb crystal clock with 2.5×10^{-18} systematic uncertainty, Phys. Rev. Lett. **134**, 023201 (2025).
[5] M. Biercuk, J. Britton, H. Uys, A. Vandevender, and J. Bollinger, Yocto-newton force detection sensitivity using trapped ions, Nat. Nanotechnol. **5**, 646 (2010).
[6] B. Deng, M. Göb, B. A. Stickler, M. Masuhr, K. Singer, and D. Wang, Amplifying a zeptonewton force with a single-ion nonlinear oscillator, Phys. Rev. Lett. **131**, 153601 (2023).
[7] R. Blatt and D. Wineland, Entangled states of trapped atomic ions, Nature (London) **453**, 1008 (2008).
[8] C. D. Bruzewicz, J. Chiaverini, R. McConnell, and J. M. Sage, Trapped-ion quantum computing: Progress and challenges, Appl. Phys. Rev. **6**, 021314 (2019).
[9] S. Willitsch, Chemistry with controlled ions, Adv. Chem. Phys. **162**, 307 (2017).
[10] M. Tomza, K. Jachymski, R. Gerritsma, A. Negretti, T. Calarco, Z. Idziaszek, and P. S. Julienne, Cold hybrid ion-atom systems, Rev. Mod. Phys. **91**, 035001 (2019).
[11] P. O. Schmidt, T. Rosenband, C. Langer, W. M. Itano, J. C. Bergquist, and D. J. Wineland, Spectroscopy using quantum logic, Science **309**, 749 (2005).
[12] M. Sinhal, Z. Meir, K. Najafian, G. Hegi, and S. Willitsch, Quantum-nondemolition state detection and spectroscopy of single trapped molecules, Science **367**, 1213 (2020).
[13] M. Sinhal and S. Willitsch, Molecular-ion quantum technologies, in *Photonic Quantum Technologies*, edited by M. Benyoucef (John Wiley & Sons, Ltd., Weinheim, Germany, 2023), Chap. 13, pp. 305–332.
[14] D. Hunger, S. Camerer, M. Korppi, A. Jöckel, T. Hänsch, and P. Treutlein, Coupling ultracold atoms to mechanical oscillators, Compt. Rend. Phys. **12**, 871 (2011).
[15] M. Aspelmeyer, T. J. Kippenberg, and F. Marquardt, Cavity optomechanics, Rev. Mod. Phys. **86**, 1391 (2014).
[16] N. Ghaemi, A. Nikoobin, and M. R. Ashory, A comprehensive categorization of micro/nanomechanical resonators and their practical applications from an engineering perspective: A review, Adv. Elect. Materials **8**, 2200229 (2022).
[17] S. Singh, M. Bhattacharya, O. Dutta, and P. Meystre, Coupling nanomechanical cantilevers to dipolar molecules, Phys. Rev. Lett. **101**, 263603 (2008).
[18] A. Sanz-Mora, S. Wüster, and J.-M. Rost, On-chip quantum tomography of mechanical nanoscale oscillators with guided Rydberg atoms, Phys. Rev. A **96**, 013855 (2017).
[19] M. Weegen, M. Poggio, and S. Willitsch, Coupling trapped ions to a nanomechanical oscillator, Phys. Rev. Lett. **133**, 223201 (2024).
[20] U. Delić, M. Reisenbauer, K. Dare, D. Grass, V. Vuletić, N. Kiesel, and M. Aspelmeyer, Cooling of a levitated nanoparticle to the motional quantum ground state, Science **367**, 892 (2020).
[21] J. Millen, T. S. Monteiro, R. Pettit, and A. N. Vamivakas, Optomechanics with levitated particles, Rep. Prog. Phys. **83**, 026401 (2020).
[22] F. Tebbenjohanns, M. L. Mattana, M. Rossi, M. Frimmer, and L. Novotny, Quantum control of a nanoparticle optically levitated in cryogenic free space, Nature (London) **595**, 378 (2021).
[23] D. S. Bykov, L. Dania, F. Goschin, and T. E. Northup, Nanoparticle stored with an atomic ion in a linear Paul trap, Phys. Rev. Lett. **135**, 213602 (2025).
[24] B. M. Zwickl, W. E. Shanks, A. M. Jayich, C. Yang, A. C. Bleszynski Jayich, J. D. Thompson, and J. G. E. Harris, High quality mechanical and optical properties of commercial silicon nitride membranes, Appl. Phys. Lett. **92**, 103125 (2008).
[25] K. Hammerer, K. Stannigel, C. Genes, P. Zoller, P. Treutlein, S. Camerer, D. Hunger, and T. W. Hänsch, Optical lattices with micromechanical mirrors, Phys. Rev. A **82**, 021803(R) (2010).
[26] M. Bild, M. Fadel, Y. Yang, U. von Lüpke, P. Martin, A. Bruno, and Y. Chu, Schrödinger cat states of a 16-microgram mechanical oscillator, Science **380**, 274 (2023).
[27] S. Camerer, M. Korppi, A. Jöckel, D. Hunger, T. W. Hänsch, and P. Treutlein, Realization of an optomechanical interface between ultracold atoms and a membrane, Phys. Rev. Lett. **107**, 223001 (2011).
[28] N. Daniilidis and H. Häffner, Quantum interfaces between atomic and solid-state systems, Annu. Rev. Condens. Matter Phys. **4**, 83 (2013).
[29] G. Kurizki, P. Bertet, Y. Kubo, K. Mølmer, D. Petrosyan, P. Rabl, and J. Schmiedmayer, Quantum technologies with hybrid systems, Proc. Natl. Acad. Sci. USA **112**, 3866 (2015).
[30] P. N. Fountas, M. Poggio, and S. Willitsch, Classical and quantum dynamics of a trapped ion coupled to a charged nanowire, New J. Phys. **21**, 013030 (2019).
[31] T. M. Karg, B. Gouraud, C. T. Ngai, G.-L. Schmid, K. Hammerer, and P. Treutlein, Light-mediated strong coupling between a mechanical oscillator and atomic spins 1 meter apart, Science **369**, 174 (2020).
[32] A. Chowdhury, M. G. Clerc, S. Barbay, I. Robert-Philip, and R. Braive, Weak signal enhancement by nonlinear resonance control in a forced nano-electromechanical resonator, Nat. Commun. **11**, 2400 (2020).
[33] M. Weegen, P. N. Fountas, M. Poggio, and S. Willitsch, Experimental implementation of an ion-nanowire hybrid system, Rev. Sci. Instrum. **96**, 063203 (2025).
[34] Y. Wang, X. Zhang, Y. Feng, R. Shao, X. Xiong, X. Fang, Y. Deng, and W. Xu, Characterization of geometry deviation effects on ion trap mass analysis: A comparison study, Int. J. Mass Spectrom. **370**, 125 (2014).
[35] A. Maitra, D. Leibfried, D. Ullmo, and H. Landa, Far-from-equilibrium noise-heating and laser-cooling dynamics in radio-frequency Paul traps, Phys. Rev. A **99**, 043421 (2019).
[36] N. Akerman, S. Kotler, Y. Glickman, Y. Dallal, A. Keselman, and R. Ozeri, Single-ion nonlinear mechanical oscillator, Phys. Rev. A **82**, 061402(R) (2010).
[37] G. H. Low, P. F. Herskind, and I. L. Chuang, Finite-geometry models of electric field noise from patch potentials in ion traps, Phys. Rev. A **84**, 053425 (2011).
[38] J. P. Home, D. Hanneke, J. D. Jost, D. Leibfried, and D. J. Wineland, Normal modes of trapped ions in the presence of anharmonic trap potentials, New J. Phys. **13**, 073026 (2011).

[39] M. Johanning, Isospaced linear ion strings, Appl. Phys. B **122**, 71 (2016).
[40] T. Gudjons, P. Seibert, and G. Werth, Influence of anharmonicities of a Paul trap potential on the motion of stored ions, Appl. Phys. B **65**, 57 (1997).
[41] S. S. Sharma and N. K. Sharma, The Schrödinger cat state of trapped ions in harmonic and anharmonic oscillator traps, J. Phys. B: At. Mol. Opt. Phys. **35**, 1643 (2002).
[42] L. M. A. Nguyen, B. Bowers, and S. Mouradian, The effect of trap design on the scalability of trapped-ion quantum technologies, Entropy **27**, 576 (2025).
[43] P. T. Grochowski, H. Pichler, C. A. Regal, and O. Romero-Isart, Quantum control of continuous systems via nonharmonic potential modulation, Quantum **9**, 1824 (2025).
[44] A. H. Nayfeh and D. T. Mook, *Nonlinear Oscillations* (John Wiley & Sons, Ltd., New York, 1995).
[45] M. Drewsen, A. Mortensen, R. Martinussen, P. Staanum, and J. L. Sørensen, Nondestructive identification of cold and extremely localized single molecular ions, Phys. Rev. Lett. **93**, 243201 (2004).
[46] F. G. Major, V. N. Gheorghe, and G. Werth, *Charged Particle Traps* (Springer, Berlin, 2005).
[47] H. J. Metcalf and P. van der Straten, *Laser Cooling and Trapping* (Springer, New York, 1999).
[48] H. Duifhuis, Nonlinear tools, in *Cochlear Mechanics: Introduction to a Time Domain Analysis of the Nonlinear Cochlea* (Springer, New York, 2008), Chap. 9, pp. 211–235.
[49] S. Zaitsev, O. Shtempluck, E. Buks, and O. Gottlieb, Nonlinear damping in a micromechanical oscillator, Nonlinear Dyn. **67**, 859 (2012).
[50] S. J. Elliott, M. G. Tehrani, and R. S. Langley, Nonlinear damping and quasi-linear modelling, Philos. Trans. R. Soc. A **373**, 20140402 (2015).
[51] D. J. Berkeland, J. D. Miller, J. C. Bergquist, W. M. Itano, and D. J. Wineland, Minimization of ion micromotion in a Paul trap, J. Appl. Phys. **83**, 5025 (1998).
[52] B. Wang, J. W. Zhang, Z. H. Lu, and L. J. Wang, Direct measurement of micromotion speed in a linear quadrupole trap, J. Appl. Phys. **108**, 013108 (2010).
[53] R. Lifshitz and M. C. Cross, *Nonlinear Dynamics of Nanomechanical and Micromechanical Resonators* (John Wiley & Sons, Ltd., Weinheim, Germany, 2008), Chap. 1, pp. 1–52.
[54] T. Barois, S. Perisanu, P. Vincent, S. T. Purcell, and A. Ayari, Frequency modulated self-oscillation and phase inertia in a synchronized nanowire mechanical resonator, New J. Phys. **16**, 083009 (2014).
[55] D. Younesian, E. Esmailzadeh, and R. Sedaghati, Existence of periodic solutions for the generalized form of Mathieu equation, Nonlinear Dyn. **39**, 335 (2005).
[56] G. T. Abraham and A. Chatterjee, Approximate asymptotics for a nonlinear Mathieu equation using harmonic balance based averaging, Nonlinear Dyn. **31**, 347 (2003).
[57] M. Sudakov, Effective potential and the ion axial beat motion near the boundary of the first stable region in a nonlinear ion trap, Int. J. Mass Spectrom. **206**, 27 (2001).
[58] I. Filippov and M. Sudakov, Analysis of electric fields in mass spectrometry, Int. J. Mass Spectrom. **467**, 116620 (2021).
[59] L. D. Landau and E. M. Lifshitz, *Course of Theoretical Physics, Mechanics*, 3rd ed. (Butterworth-Heinemann, Oxford, UK, 1976), Vol. 1.
[60] D. Leibfried, R. Blatt, C. Monroe, and D. Wineland, Quantum dynamics of single trapped ions, Rev. Mod. Phys. **75**, 281 (2003).
[61] https://docs.scipy.org/doc/scipy/reference/generated/scipy.integrate.solve_ivp.html.
[62] J. Dormand and P. Prince, A family of embedded Runge-Kutta formulae, J. Comput. Appl. Math. **6**, 19 (1980).
[63] J. Pedregosa-Gutierrez, C. Champenois, M. R. Kamsap, and M. Knoop, Ion transport in macroscopic rf linear traps, Int. J. Mass Spectrom. **381-382**, 33 (2015).
[64] M. Feldman, *Hilbert Transform Applications in Mechanical Vibration* (Wiley, 2011).